Soil Dynamics and Earthquake Engineering 76 (2015) 86–99

Contents lists available at ScienceDirect

Soil Dynamics and Earthquake Engineering

journal homepage: www.elsevier.com/locate/soildyn

Seismic dynamics of offshore breakwater on liquefiable seabed foundation

Jianhong Ye [a,1], Gang Wang [b,*]

[a] State Key Laboratory of Geomechanics and Geotechnical Engineering, Institute of Rock and Soil Mechanics, Chinese Academy of Sciences, Wuhan 430071, China

[b] Department of Civil and Environmental Engineering, Hong Kong University of Science and Technology Clear Water Bay, Kowloon, Hong Kong SAR, China

ARTICLE INFO

Article history:
Received 10 July 2014
Received in revised form
13 November 2014
Accepted 1 February 2015
Available online 18 February 2015

Keywords:
Offshore breakwater
Numerical simulation
Seabed–structure interaction
Liquefaction
Seismic dynamics

ABSTRACT

Offshore structures, such as composite breakwaters, are generally vulnerable to strong seismic wave propagating through loose or medium-dense seabed foundation. However, the seismically induced failure process of offshore structures is not well understood. In this study, seismic dynamics of a composite breakwater on liquefiable seabed foundation is investigated using a fully coupled numerical model FSSI-CAS 2D. The computation results show that the numerical model is capable of capturing a variety of nonlinear interaction phenomena between the composite breakwater and its seabed foundation. The numerical investigation demonstrates a three-stage failure process of the breakwater under seismic loading. In this process, the far-field seabed can become fully liquefied first, inducing excessive settlement of the structure, followed by significant lateral movement and tilting of the structure when the near-field soil progressively liquefies. The study demonstrates great promise of using advanced numerical analysis in geotechnical earthquake design of offshore structures.

© 2015 Elsevier Ltd. All rights reserved.

1. Introduction

Composite breakwaters have been widely constructed as a kind of coastal defense structure to protect ports and harbors. Engineers mainly concern about the stability of these offshore structures under environmental loading, such as ocean waves and earthquakes. A detailed review on the dynamic response of breakwaters under wave loading can be found in [1]. On the other hand, devastating damage to offshore structures has been recorded in the past earthquakes, including failure of offshore structures in Los Angeles (USA) in 1994, Kobe (Japan) in 1995, Kocaeli (Turkey) in 1999, Athens (Greece) in 1999 and Sumatra (Indonesia) in 2003 for examples [2–7]. Therefore, seismic analysis should be well considered for important offshore structures built in active seismic regions.

To date, experimental and numerical investigations on seismic dynamics of offshore structures are still limited. Among limited literature, Yuksel et al. [6] analyzed the earthquake-induced deformation of a breakwater at the Eregli Fishery port during the 1999 Koceali Turkey earthquake. Kiara et al. [8] and Memos et al. [9] conducted a series of experimental tests to investigate the seismic response and stability of a rubble-mound breakwater on a shaking table. In their experiment, they found the response acceleration is negatively correlated to the buried depth in sandy bed, and the sandy bed deformation played a dominant role in breakwater failure. Numerical analysis was also performed in their study, where the dynamic water pressure acting on outer surface of the rubble-mound breakwater was considered using Westerggard formulation. Similar shaking table tests were also conducted by Ozaki and Nagao [10]. Mohajeri et al. Earthquake-induced sliding displacement of a caisson wall was also studied in a shaking table test [11].

Based on the work of [8,9], numerical analysis of seismic response of a rubble-mound breakwater was performed using a coupled numerical model [12]. However, the input excitation is only a harmonic motion, not a real seismic wave. The finite difference program FLAC^{2D} was also adopted to estimate the permanent displacement of a rubble-mound breakwater on a sandy bed under seismic wave loading [13]. In their study, the Mohr–Coulomb constitutive model and the pore pressure built-up model proposed in [14] were used. Obviously, soils and pore water are not coupled in their analysis. Recently, deformation of a rubble-mound breakwater under horizontal harmonic motion was also experimentally and numerically investigated [15]. However, the seabed foundation is not considered as a part of the analysis.

In engineering practice, newly deposited Quaternary sediments are often encountered in offshore areas, and a great number of offshore structures have been constructed on these materials. Under seismic loading, the seabed foundation may liquefy due to progressive build up of residual pore pressure. As a result, the overlying offshore structures could translate, tilt, or even collapse.

* Corresponding author.
E-mail address: gwang@ust.hk (G. Wang).
[1] Formerly at HKUST.

http://dx.doi.org/10.1016/j.soildyn.2015.02.003
0267-7261/© 2015 Elsevier Ltd. All rights reserved.

Therefore, studying the liquefaction behaviors of the seabed foundation is important in the seismic design of offshore structures. In the past 30 years, significant progress has been made to advance the state-of-the-art modeling of liquefiable soils [17–23]. However, these advanced models have not yet been used to study the nonlinear interaction mechanism of offshore structures with seabed foundation. Most of the previous investigations on seismic dynamics of offshore structures used simple constitutive models such as elastic [24,25] or Mohr–Coulomb model to model the seabed soil. These simple models are not capable of simulating the complicated nonlinear cyclic behaviors of soils and failure process of offshore structures. Intensive nonlinear interaction between seabed foundation and the structure can not be effectively captured. Iai et al. [16] conducted effective stress analyses of port structures in Kobe port during the Hyogoken–Nambu earthquake in 1995. The numerical analyses calculated that the composite breakwater constructed on loose seabed soil settled about 2 m during the event, which is consistent with the field observation. The work highlighted the importance of using effective stress analyses with well-calibrated cyclic soil model to realistically capture the nonlinear structure–seabed interaction.

In this study, the seismic dynamics of a composite breakwater on liquefiable seabed foundation is investigated using a fully coupled numerical model FSSI-CAS 2D. An advanced soil constitutive model – Pastor-Zienkiewics Mark III (PZIII) [17] is used to describe the complicated nonlinear dynamic behavior of the seabed soil. The variation of void ratio and corresponding change in the permeability of the soil are considered in the simulation. Additionally, the hydrostatic pressure acting on outer surface of the composite breakwater and its seabed foundation is updated in real time in accordance to the movement of the composite breakwater and the deformation of seabed foundation. A real recorded seismic wave off Pacific coast in the event of March 11, 2011 Tohoku-Oki earthquake in Japan is adopted as the input motion. The computational results show that the coupled numerical model FSSI-CAS 2D is capable of capturing the progressive liquefaction of the far-field and near-field seabed soil, as well as subsidence, translation and tilting of the composite breakwater in the failure process.

2. Coupled numerical model: FSSI-CAS 2D

2.1. Governing equations

The dynamic Biot's equation, known as "$u-p$" approximation proposed in [26], is used to describe the dynamic response of the porous medium under earthquake loading. In this formulation, the relative displacements of pore fluid to soil particles are ignored, but the acceleration of the pore water and soil particles are included:

$$\frac{\partial \sigma_x'}{\partial x}+\frac{\partial \tau_{xz}}{\partial z}=-\frac{\partial p_s}{\partial x}+\rho\frac{\partial^2 u_s}{\partial t^2}, \tag{1}$$

$$\frac{\partial \tau_{xz}}{\partial x}+\frac{\partial \sigma_z'}{\partial z}+\rho g=-\frac{\partial p_s}{\partial z}+\rho\frac{\partial^2 w_s}{\partial t^2}, \tag{2}$$

$$k\nabla^2 p_s-\gamma_w n\beta\frac{\partial p_s}{\partial t}+k\rho_f\frac{\partial^2 \epsilon_v}{\partial t^2}=\gamma_w\frac{\partial \epsilon_v}{\partial t}, \tag{3}$$

where (u_s, w_s) are displacements of the soil in horizontal and vertical directions, respectively; n is soil porosity; σ_x' and σ_z' are effective normal stresses in the horizontal and vertical directions, respectively; τ_{xz} is shear stress; p_s is the pore water pressure; $\rho=\rho_f n+\rho_s(1-n)$ is the average density of porous seabed; ρ_f is the fluid density; ρ_s is solid density; k is the Darcy's permeability; g is the gravitational acceleration; γ_ω is unit weight of the water and ϵ_v is the volumetric strain. In Eq. (3), the compressibility of pore fluid β and the volume strain ϵ_v are defined as

$$\beta=\left(\frac{1}{K_f}+\frac{1-S_r}{p_{w0}}\right) \quad \text{and} \quad \epsilon_v=\frac{\partial u_s}{\partial x}+\frac{\partial w_s}{\partial z}, \tag{4}$$

where S_r is the degree of saturation of seabed, p_{w0} is the absolute static pressure and K_f is the bulk modulus of pore water. In general, $K_f=2.24\times10^6$ kPa.

The finite element method is used to solve the above governing equations (1)–(3). The discretized governing equations are

$$\mathrm{M}\ddot{\mathbf{u}}+\mathrm{K}\mathbf{u}-\mathrm{Q}\mathbf{p}=f^{(1)} \tag{5}$$

$$\mathrm{G}\ddot{\mathbf{u}}+\mathrm{Q}^{\mathrm{T}}\ddot{\mathbf{u}}+\mathrm{S}\dot{\mathbf{p}}+\mathrm{H}\mathbf{p}=f^{(2)} \tag{6}$$

The Generalized Newmark pth order scheme for jth order equation is adopted as the numerical integrator when solving the above discretized equations. The definition of coefficient matrices M, K, Q, G, S, H, $f^{(1)}$, $f^{(2)}$, and the detailed information for the numerical method to solve the Biot's equation can be found in [1,27–29]. In this seismic dynamics simulation, the stiffness-proportional Rayleigh damping model is applied for the purpose of stabilizing the numerical results. In computation, $\alpha=0$, and $\beta=0.0003$ is chosen as used in [30]. In this study, large deformation occurs in loose liquefiable seabed under the earthquake shaking. The updated Lagrangian method is adopted to handle the large deformation problem. The coordinates of nodes, variables dependent on the effective stress history, such as void ratio e and permeability k, are updated in each time step based on deformation. Correspondingly, the coefficient matrices M, K, Q, G, S, H, $f^{(1)}$, $f^{(2)}$, as well as prescribed boundary values are also updated.

From the physics point of view, the void ratio e and related Darcy's permeability k vary according to the deformation of granular materials. In most previous studies, this variation process is not considered based on the assumption of small deformation. In this study, large deformation occurs in the seabed foundation under seismic loading. Therefore, variation of void ratio e and permeability k cannot be ignored in the near-field region, i.e., the seabed foundation close to the offshore breakwater. The practice of numerical implementation in this study indicated that the void ratio and permeability should be updated in each time step following the deformation of the soil. Otherwise, non-convergence may be encountered in the numerical analysis. Using large deformation assumption, the void ratio e is updated in each time step according to the following expression:

$$e_{n+1}=(1+e_n)\exp\left(\frac{\Delta p}{Q}+\Delta\epsilon_v\right)-1 \tag{7}$$

where Q is the compressibility of pore water, Δp is the pore pressure increment and $\Delta\epsilon_v$ is the volumetric strain increment of the soil in this time increment. Accordingly, Darcy's permeability k can be updated [31]:

$$k_{n+1}=C_f\frac{e_{n+1}^3}{1+e_{n+1}} \tag{8}$$

in which C_f is an empirical coefficient, depending on the dynamic viscosity, size and arrangement of soil particles. Recently, [32] also proposed a similar equation to relate e and k based on the fractal characteristics of pore space geometry. If the initial void ratio e_0 and permeability k_0 are known, the empirical coefficient C_f can be back-calculated as [33]

$$C_f=k_0\frac{1+e_0}{e_0^3} \tag{9}$$

2.2. Constitutive model: Pastor–Zienkiewics–Mark III

Based on classical plasticity theory [34], the constitutive relationship for the effective stress and strain of the soil can be

written as

$$\sigma'_{ij} = D^{ep}_{ijkl}\epsilon_{kl} \tag{10}$$

where ϵ_{kl} is the strain of soil, D^{ep}_{ijkl} is the elasto-plastic modulus:

$$D^{ep}_{ijkl} = D^{e}_{ijkl} - \frac{D^{e}_{ijmn}m_{mn}n_{st}D^{e}_{stkl}}{H_{L/U} + n_{st}D^{e}_{stkl}m_{kl}} \tag{11}$$

where $D^{e}_{ijkl} = 2G(\delta_{ik}\delta_{jl} + \nu/(1-2\nu)\delta_{ij}\delta_{kl})$, G and ν are the elastic shear modulus and Poisson's ratio, respectively. $H_{L/U}$ is the plastic modulus at loading or unloading stage. m_{mn} is a unit tensor for the plastic flow direction, n_{st} is the unit tensor for loading or unloading direction. The above directional tensors are formulated as

$$m_{mn} = \frac{\left(\frac{\partial g}{\partial \sigma'_{mn}}\right)}{\left\|\frac{\partial g}{\partial \sigma'_{mn}}\right\|} \quad \text{and} \quad n_{st} = \frac{\left(\frac{\partial f}{\partial \sigma'_{st}}\right)}{\left\|\frac{\partial f}{\partial \sigma'_{st}}\right\|} \tag{12}$$

where $\|\cdot\|$ represents tensor norm, f and g are the yield function and plastic potential function in stress space. An associated flow rule will be implied if f=g. Otherwise, a non-associated flow rule will be applied.

In this study, the elasto-plastic constitutive model PZIII, proposed by [17] based on the generalized plastic theory, is adopted to describe the dynamic behavior of loose seabed foundation under seismic wave. In PZIII, the yield surface function f and plastic potential surface function g are defined as

$$f = q' - M_f p'\left(1 + \frac{1}{\alpha_f}\right)\left[1 - \left(\frac{p'}{p'_f}\right)^{\alpha_f}\right] = 0 \tag{13}$$

$$g = q' - M_g p'\left(1 + \frac{1}{\alpha_g}\right)\left[1 - \left(\frac{p'}{p'_g}\right)^{\alpha_g}\right] = 0 \tag{14}$$

The plastic modulus at loading and unloading stage are defined as

$$H_L = H_0 p'\left(1 - \frac{q'/p'}{\eta_f}\right)^4\left[1 - \frac{q'/p'}{M_g} + \beta_0\beta_1\exp(-\beta_0\xi)\right]\left(\frac{q/p'}{\eta_{max}}\right)^{-\gamma_{DM}} \tag{15}$$

$$H_U = \begin{cases} H_{u0}\left(\frac{M_g}{\eta_u}\right)^{\gamma_U} & \text{for } \left|\frac{M_g}{\eta_u}\right| > 1 \\ H_{u0} & \text{for } \left|\frac{M_g}{\eta_u}\right| \le 1 \end{cases} \tag{16}$$

where the p' and q' is the mean effective stress and deviatoric stress, respectively. $\eta_f = (1+1/\alpha_f)M_f$, η_{max} is the maximum stress ratio (p'/q'), and η_u is the stress ratio at the unloading point. M_f, M_g, α_f, α_g, β_0, β_1, γ and γ_{DM} are the parameters describing the properties of sandy soil. The detailed information about the PZIII model can be found in [17] and [28]. PZIII is an excellent constitutive model to describe the behaviors of clay and sandy soil. Its reliability has been validated by a series of laboratory tests under monotonic and cyclic loading [28].

2.3. Computational domain, boundary condition and input seismic wave

The computational domain is shown in Fig. 1. It is assumed that a composite breakwater is constructed on seabed floor in the offshore environment, consisting of a caisson and a rubble mound beneath. The cassion is made of concrete, and can be practically treated as an impermeable rigid object; while the rubble mound is permeable with a large void volume. The total length of the computational domain is 636 m. The distances from the breakwater to lateral sides of the seabed foundation are both 300 m,

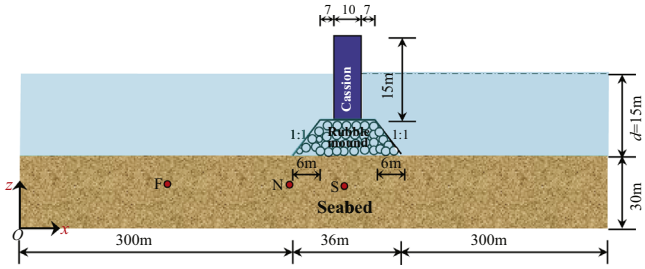

Fig. 1. Computational domain and dimension for composite breakwater and seabed foundation system.

which is considered to be large enough to minimize the influence of the lateral boundaries. In this study, the following boundary conditions are applied in computation.

(1) The bottom of seabed foundation is treated as a rigid base and it is impermeable:

$$u_s = w_s = 0 \quad \text{and} \quad \frac{\partial p_s}{\partial z} = 0 \quad \text{at } z = 0 \tag{17}$$

(2) Periodic boundary condition is applied at two lateral sides of the computational domain:

$$u_s|_{x=0\text{ m}} = u_s|_{x=636\text{ m}}, \quad w_s|_{x=0\text{ m}} = w_s|_{x=636\text{ m}},$$
$$p_s|_{x=0\text{ m}} = p_s|_{x=636\text{ m}} \tag{18}$$

(3) Hydrostatic pressure is applied on the surface of seabed and the outer surface of the composite breakwater. All force induced by the hydrostatic pressure is perpendicular to the surfaces.

It is noted that a constant water level is assumed in this study. Although seabed and structure vibration could generate small waves, dynamic pressure induced by the small wave can be neglected based on experimental tests conducted by Memos et al. [9]. In engineering practice, a large ocean wave is unlikely to occur simultaneously with a strong earthquake. Therefore, the wave loading is not considered.

In this study, we consider variation of hydrostatic pressure acting on breakwater and its seabed foundation in large deformation process. Numerical results indicate that the breakwater could experience horizontal translation up to 12 m, subsidence of 6 m, and tilting of 15 °. The complex dynamics of the breakwater makes the hydrostatic pressure acting on it and on its seabed foundation change significantly during seismic loading. The practice of numerical implementation indicated that the numerical analysis will not converge if the variation of hydrostatic pressure acting on the breakwater and seabed foundation is not updated as boundary values following the deformation of seabed and breakwater in computation. In each time step, the hydrostatic pressure acting on breakwater and its seabed foundation is updated as

$$p_s = \rho_f g(d_0 + d_v) \tag{19}$$

where d_0 is the initial water depth and d_v is the vertical subsidence of the seabed surface and outer surface of the breakwater.

(4) Since the concrete cassion is impermeable, an upward buoyant force acts on the bottom of concrete caisson. Neglecting this buoyant force leads to overestimation of the initial stresses in the seabed foundation and subsidence of the breakwater [35,36].

In this study, real seismic waves recorded in the 2011 (M_w, 9.0) Tohoku earthquake are selected as the input motions. This seismograph station MYGH03 (141.6412E, 38.9178N) is located near Pacific coast at an epicenter distance of 154 km, representing real seismic waves propagating from the source to the offshore foundation. In order to capture the nonlinear soil responses and site amplification, wave traces recorded by the downhole seismograph are used. Baseline correction and noncasual butterworth filtering are applied to the acceleration time histories, with a high-pass frequency of 0.03 Hz

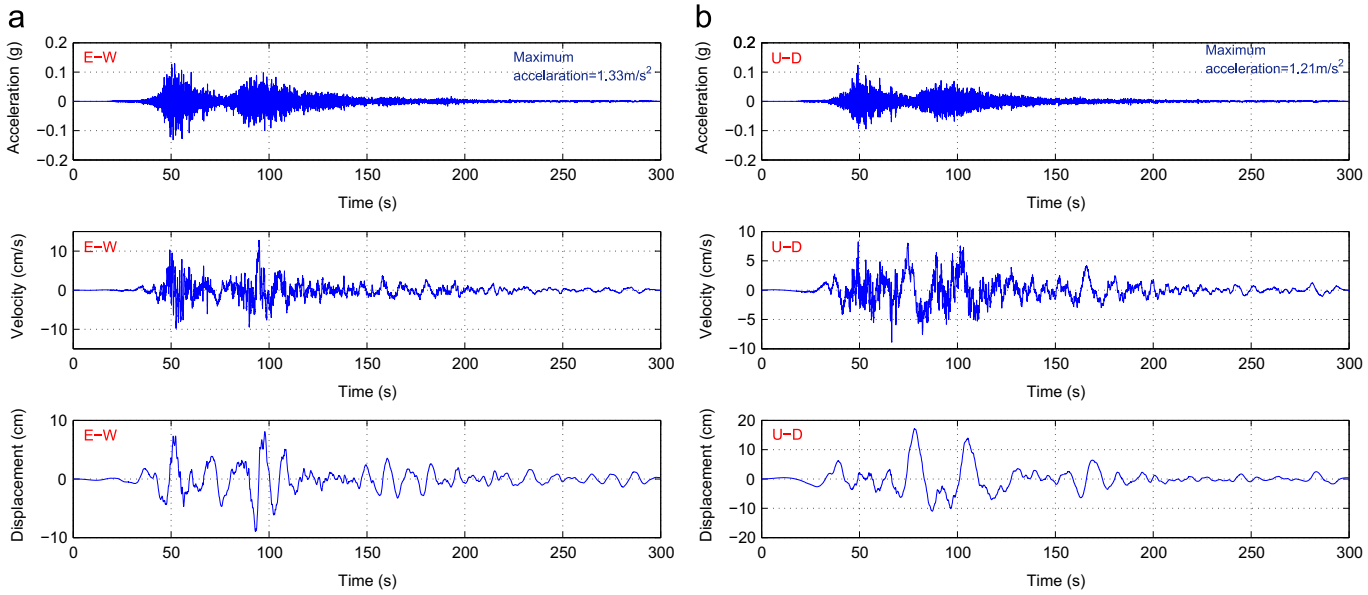

Fig. 2. Input seismic wave as recorded at downhole station MYGH03 during the 2011 Tohoku earthquake in Japan. (a) E–W. (b) U–D.

Table 1
PZIII model parameters for seabed soils.

Parameter	Nevada sand	Unit
K_{evo}	2000	kPa
G_{eso}	2600	kPa
p'_0	4	kPa
M_g	1.32	–
M_f	1.3	–
α_f	0.45	–
α_g	0.45	–
β_0	4.2	–
β_1	0.2	–
H_0	750	–
H_{U0}	40,000	kPa
γ_u	2.0	–
γ_{DM}	4.0	–

Table 2
Properties of composite breakwater and its seabed foundation in seismic analysis.

Medium	E (kPa)	ν	k (m/s)	n	S_r
Rubble mound	1.0×10^6	0.33	2.0×10^{-1}	0.4	0.99
Caisson	1.0×11^9	0.25	1.0×10^{-12}	0.0	0.0
Seabed	–	0.33	1.0×10^{-5}	0.4	0.98

and a low-pass of frequency 30 Hz. The post-processing removes high-frequency noise, and keeps the usable period of records up to 30 s. The acceleration time histories are applied simultaneously in the horizontal (E–W) and vertical (U–D) directions at the bottom of the computational domain. As shown in Fig. 2, the peak acceleration is 0.14 g in E-W direction and 0.12 g in U-D direction, respectively.

2.4. Initial consolidation of breakwater-seabed foundation system

Considering a composite breakwater built on newly deposited Quaternary sediments in offshore environment, parameters of the soil used in PZIII model are listed in Table 1, which were determined for a medium-dense Nevada sand (D_r=60%) in VELACS project [28]. Due to the fact that plastic deformation usually would not occur in the concrete caisson and rubble mound, they are modeled as elastic media in this study as listed in Table 2. Finally, the water depth d=15 m is assumed in the analysis.

In the offshore environment, the seabed soil usually has experienced consolidation under self-weight and seawater loading in sedimentation process. Additionally, after the breakwater is constructed, the seabed close to the composite breakwater will be loaded under the weight of the breakwater. This leads to the generation of excess pore pressure in the seabed foundation at the early stage, and dissipation of excess pore pressure with time. Meanwhile, the composite breakwater subsides downward, until a new balanced state is reached. In order to simulate the seismic dynamics of breakwater and its seabed foundation, the initial in-situ stress state of the seabed foundation and breakwater should be determined first, as the initial condition for the following seismic analysis.

Fig. 3 shows the distributions of horizontal and vertical displacements, effective stress and pore pressure in the seabed foundation after the consolidation (note only the section in the range of 200–400 m is shown). After consolidation, the composite breakwater subsides about 15 cm, and the soil is compressed and displaced toward two lateral sides. The lateral displacement is only 1.2–1.6 cm, much smaller than the vertical subsidence. It can be seen from Fig. 3 that the contours of pore pressure in the seabed foundation are layered, which is consistent with the distribution of hydrostatic water pressure over depth. The effective stresses in the seabed foundation under the composite breakwater increase significantly comparing with the far-field condition (where there is no offshore structure). Additionally, there are two shear-stress concentration zones in the seabed close to the two sides of the rubble mound, with the maximum shear stress over 70 kPa. The detailed analysis about the consolidation of seabed foundation under hydrostatic pressure and gravity of marine structures can be found in [35,36].

3. Seismic dynamics of breakwater and seabed foundation

3.1. Three-stage deformation process of breakwater-seabed system

Fig. 4 shows the deformation process of the breakwater-seabed foundation system under the earthquake wave loading. The deformation process is mainly consisted of three stages. In the first stage (t = 0–60 s), seabed soils at the far field experienced liquefaction and strength degradation under cyclic loading. In the second stage (t = 60–100 s), the breakwater structure subsides downwards, and

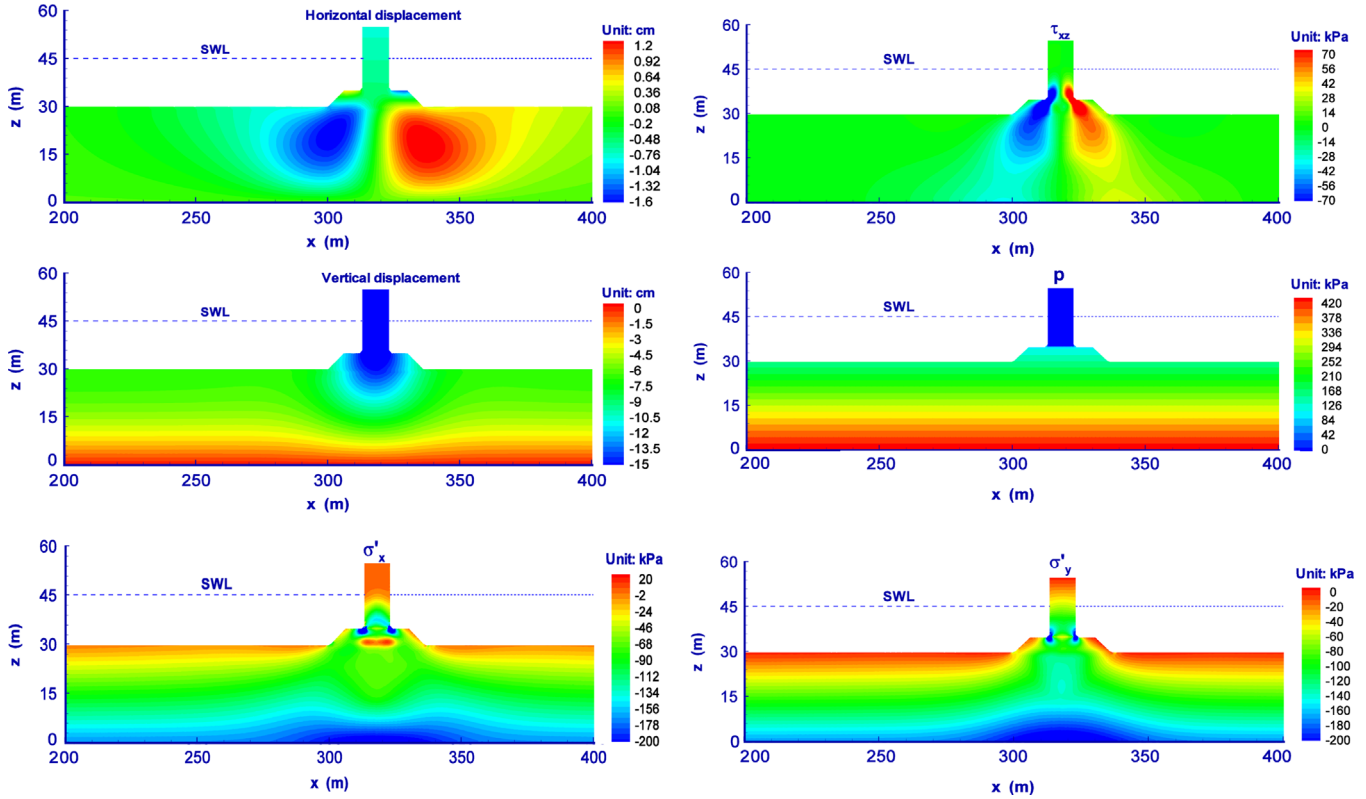

Fig. 3. Distribution of displacements, effective stress and pore pressure in the breakwater-seabed system after consolidation.

part of near-field soils liquefy. In the third stage ($t = 100$–300 s), the breakwater translates and tilts to reach a failure configuration as soils underneath the structure cannot fully support the structure.

In the following sections, we discuss the three-stage interaction mechanism of breakwater-seabed foundation system in details. We will compare the response of three representative points in the computational domain, as illustrated in Fig. 1: (1) seabed soils at the far field, represented by point F at $x=150$ m and a depth of about 10 m ($z=19.7$ m); (2) the near-field soil at point N ($x=300$ m, $z=19.7$ m) underneath the left corner of the rubble mount; (3) Point S on the symmetric line and directly beneath the composite breakwater at ($x=318$ m, $z=19.7$ m).

3.2. Stage 1: seabed liquefaction at far field

The far-field point F ($x=150$ m, $z=20$ m) is located 150 m away from the composite breakwater. Therefore, presence of the composite breakwater has little influence on seismic dynamics of the far-field soils. In Fig. 5, the pore pressure builds up quickly after the input motion arrives at the computational domain ($t \geq 20$ s). At the time $t = 60$ s, the residual pore pressure reaches its maximum value and oscillates around a constant afterwards. The pore-pressure oscillation is mainly due to volumetric compression of the pore water resulted from the vertical excitation. In the process of pore pressure build-up, the mean effective stresses in the soil I_1 decreases correspondingly. The soil is liquefied when I_1 approaches zero at $t=60$ s. After liquefaction, the soil cannot transmit shear wave, and the shear stress remains zero after 60 s.

The acceleration time histories of the seabed foundation at the far field is illustrated in Fig. 6. The acceleration reaches a peak value of 1.57 m/s^2 at about 50 s in the E–W direction. After liquefaction (60 s), the horizontal acceleration is significantly reduced as shear wave cannot be transmitted through the liquefied soil. However, the phenomenon can not be observed in the vertical (U–D) acceleration, demonstrating the liquefied soil can still transmit compressive wave effectively.

3.3. Stage 2: subsidence of breakwater and seabed liquefaction at near field

Due to the presence of the composite breakwater, seabed soils beneath and near to the composite breakwater exhibited considerably different behaviors compared with the far-field soil. When the far-field soil first reaches liquefaction at the end of stage 1 ($t = 60$ s), the lateral effective confining stress acting on the near-field soil diminishes, as shown in the mean effective stress distribution in Fig. 7. Accordingly, the soils underneath the breakwater were compressed to settle vertically and also displaced the surrounding soils laterally (up to 1–1.5 m) on the two sides, as shown in the displacement contour in Fig. 7. At the end of stage 2 ($t=100$), the subsidence of the caisson is up to 1.6 m, while there is little horizontal movement. From the figure, it is also observed the pore pressure in the seabed foundation beneath the breakwater is always smaller than that in the far field, which indicates the construction of a breakwater can constrain the development of pore pressure in the near field. The distribution of mean effective stress clearly shows that I_1 is far away from zero in the seabed foundation beneath the composite breakwater, although the mean effective stress already reaches zero in the far field when $t=100$ s. The variation process of pore pressure, effective stresses and void ratio at near-field point N is shown in Fig. 9, which is significantly different from that at the far-field. The pore pressure at point N ($x=300$ m, $z=19.7$ m) also builds up quickly in the first stage (till 60 s). However, large overburden pressure from the overlying structure postponed the liquefaction process of the near-field soil. Liquefaction would not occur beneath the edge of the rubble mount until 100 s, as is evidenced by the reduction of the mean effective stress I_1 and shear stress τ_{xz} to zero at that moment.

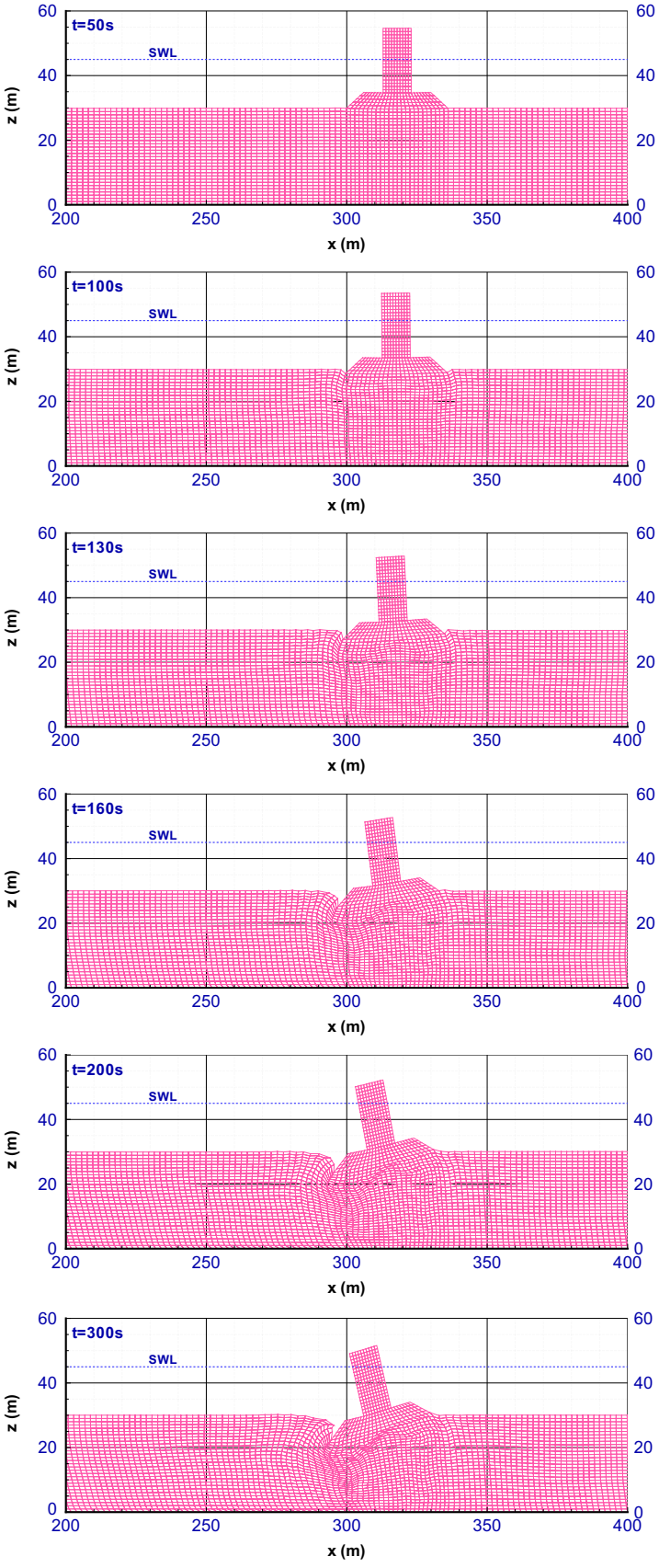

Fig. 4. Deformation process of breakwater-seabed foundation system under seismic wave loading (Note: only a portion of mesh is shown).

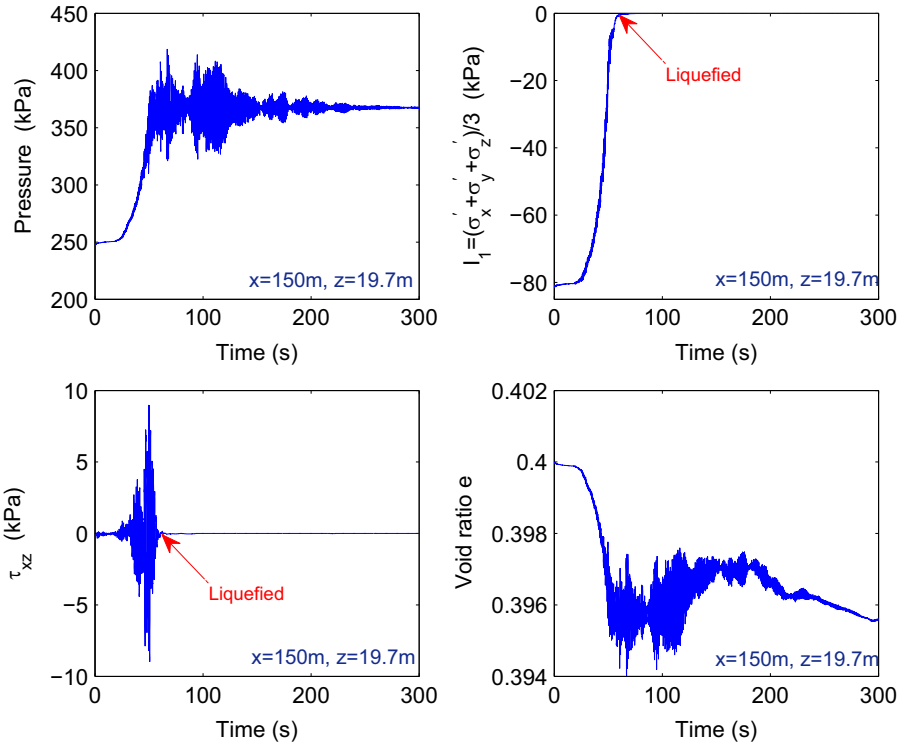

Fig. 5. Time histories of pore pressure, effective stress, and void ratio in seabed foundation at far-field point F ($x=150$ m, $z=19.7$ m).

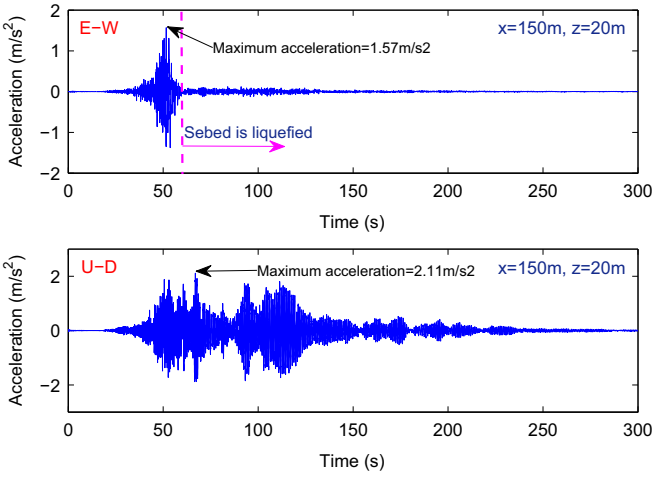

Fig. 6. Acceleration time histories in seabed at the far field, point F ($x=150$ m, $z=19.7$ m).

3.4. Stage 3: translation and tilting of breakwater

In stage 3 (after $t=100$ s), the near-field soil continues to liquefy and the non-liquefied zone underneath the breakwater is significantly reduced. Accordingly, the composite breakwater continues to subside, accompanied with tilting and large horizontal displacement to the left side. Fig. 8 shows the distribution of pore pressure, mean effective stress and displacements in the breakwater-seabed foundation system at the end of simulation ($t=300$ s). The rotation, translation and subsidence of the structure is resulted from progressive liquefaction of soils underneath the structure. In the end, one column of non-liquefied soil behaves as a buried pile to support the composite breakwater from a complete failure.

The deformation patterns of the breakwater influence the variation of pore pressure, effective stress, and void ratio in seabed foundation at the near field (point N) and soils underneath the structure (point S), as illustrated in Figs. 9 and 10. In Fig. 9, the residual pore pressure in near-field seabed foundation continue to increases to over 500 kPa after liquefaction ($t=100$ s) due to significant tilting of the composite breakwater and downward movement of the soil. As is discussed above, the composite breakwater begins to significantly displace to left side, subside downward and rotate anti-closewise at the stage 3. This movement mode makes the gravity center of the composite breakwater shifting from the symmetrical axis towards point N. After $t=170$ s, the gravity center moves further away from N. The pore pressure reduces and void ratio increases.

As shown in Fig. 10, the time histories of pore pressure, effective stresses and void ratio at point S is also significantly different from the above analysis. In stage 1, the residual pore pressure quickly builds up under seismic wave loading. During stage 2 ($t=60$–100 s), the dominant deformation of the composite breakwater is subsidence, with little horizontal movement or tilting. The effective mean stress I_1 of the soil increases in the subsiding movement, together with a significant decreases in the pore pressure during $t=60$–180 s. Starting from 100 s, tilting of composite water shifts its gravity center away from point S. We see continued decrease of pore pressure and mean effective stress. The time history of mean effective stress I_1 shows that liquefaction occurs at point S at $t=180$ s. After liquefaction, the gravitational load of breakwater is borne only by the pore water. We observe increase in pore pressure and void ratio from that moment.

4. Comparison of seismic response of far-field and near-field soils

4.1. Acceleration profile

Fig. 11 shows the acceleration time histories in seabed at point N and S. Compared with the far-field soil response (point F) in Fig. 6, considerable horizontal shear waves are transmitted to the near-field throughout the shaking. Fig. 12 demonstrates the distribution of peak

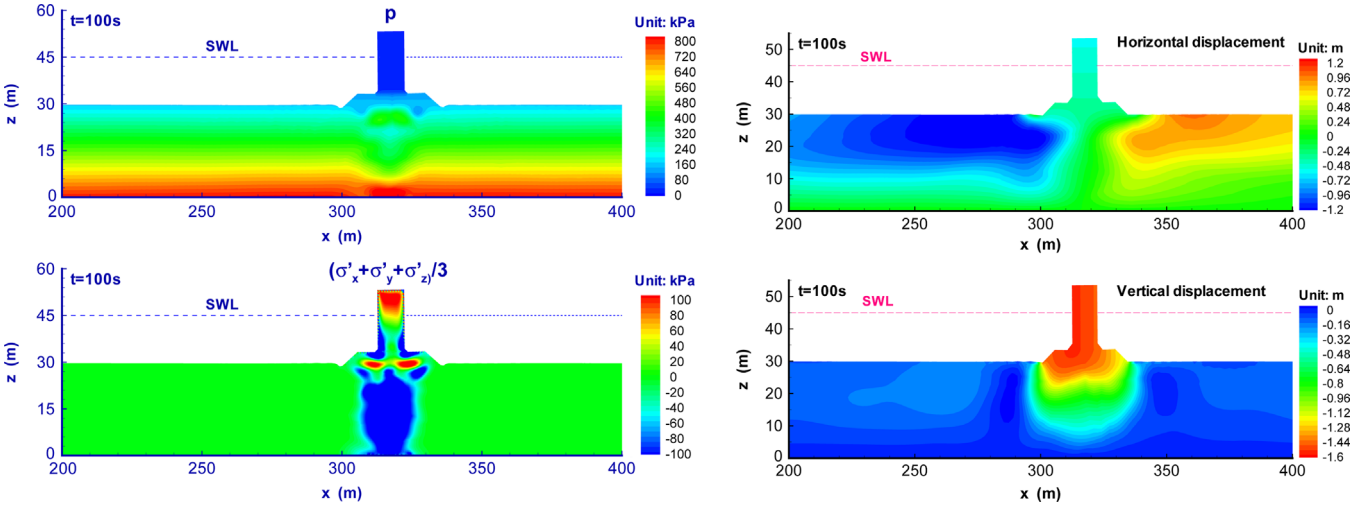

Fig. 7. Distribution of pore pressure, mean effective stress and displacements in the breakwater-seabed foundation system at $t = 100$ s.

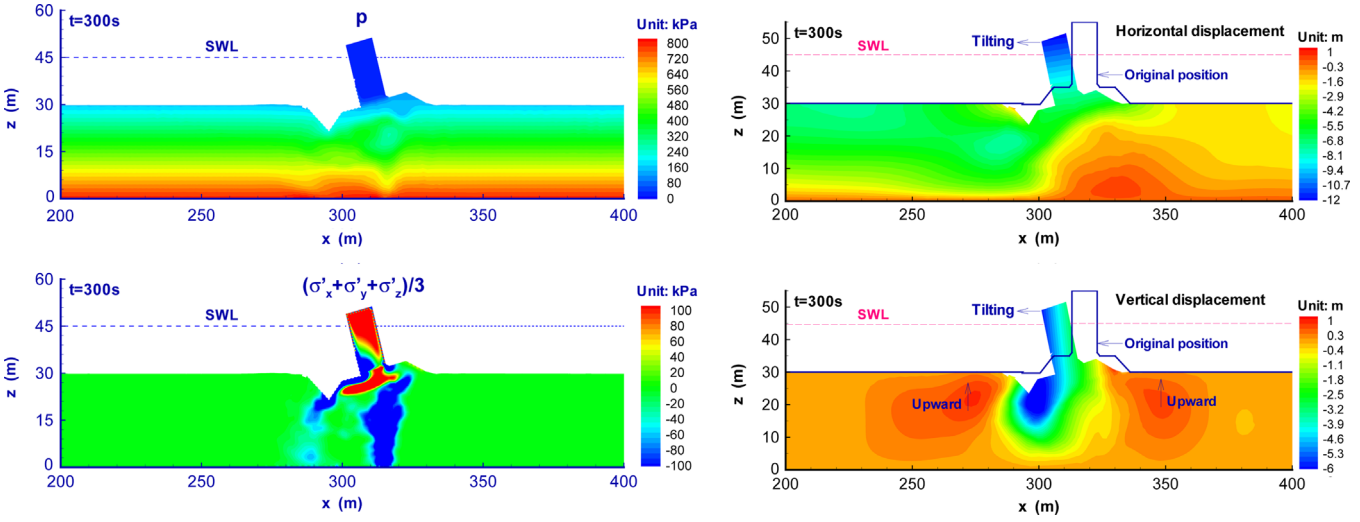

Fig. 8. Distribution of pore pressure, mean effective stress and displacements in the breakwater-seabed foundation system at $t = 300$ s.

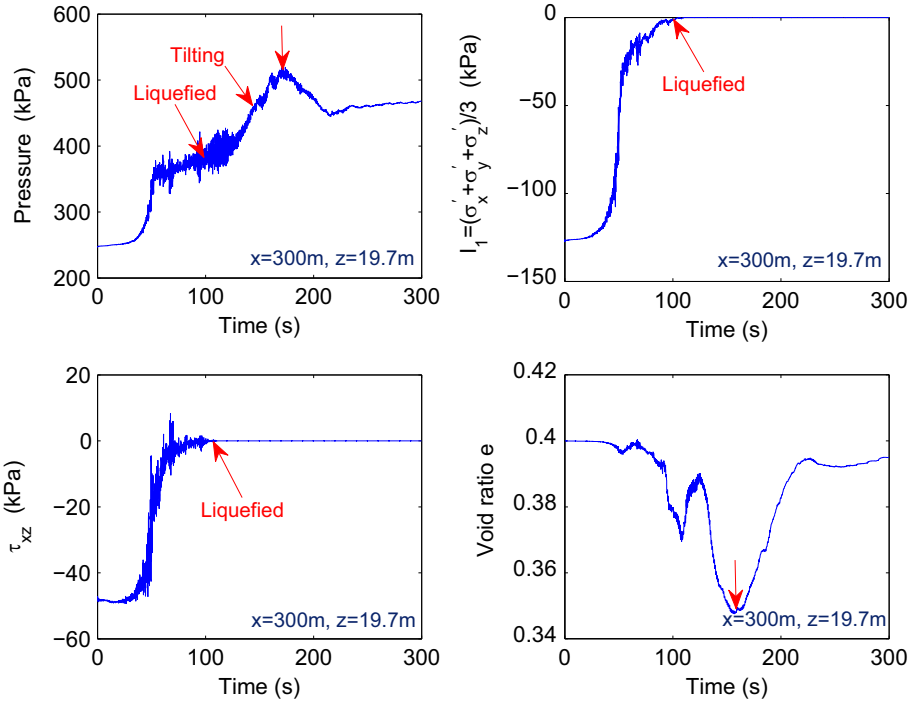

Fig. 9. Time history curve of pore pressure, effective stress, and void ratio in seabed foundation at near-field point N (x=300 m, z=19.7 m).

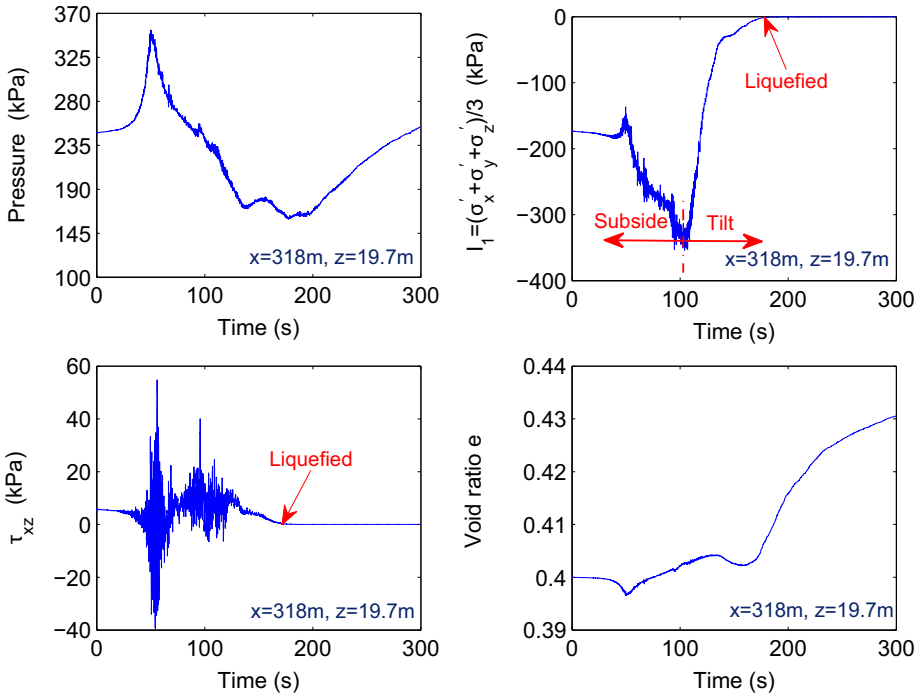

Fig. 10. Time history curve of pore pressure, effective stress, and void ratio in seabed foundation at symmetrical axis point *S* (x=318 m, z=19.7 m).

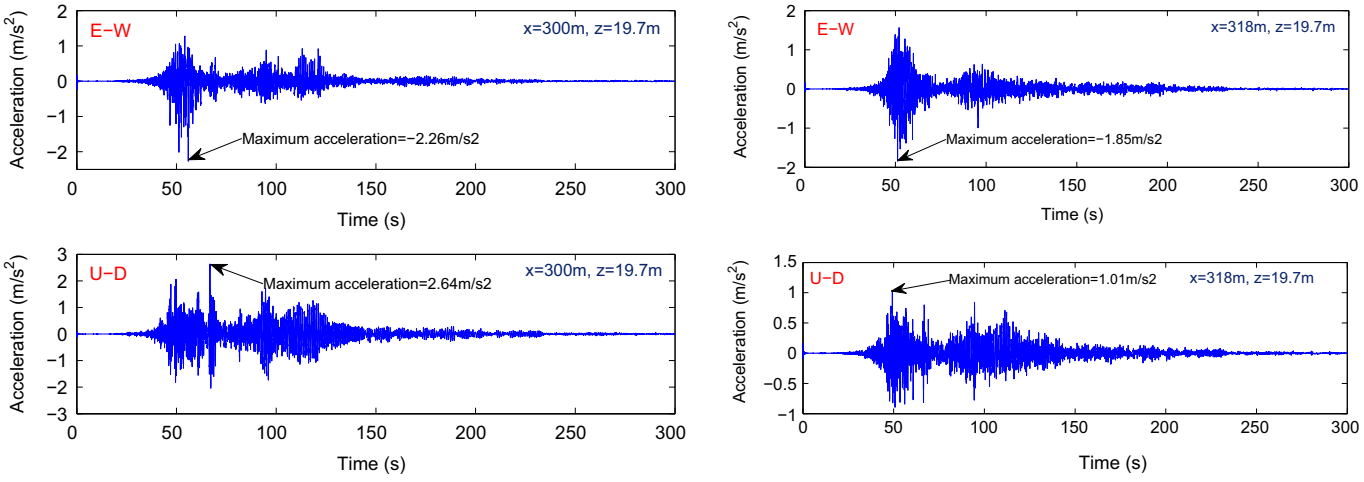

Fig. 11. Acceleration time histories in seabed (a) at the near field point *N*, (b) at the point of symmetry *S* beneath the structure. (a) Near field point *N*. (b) Point of symmetry *S*.

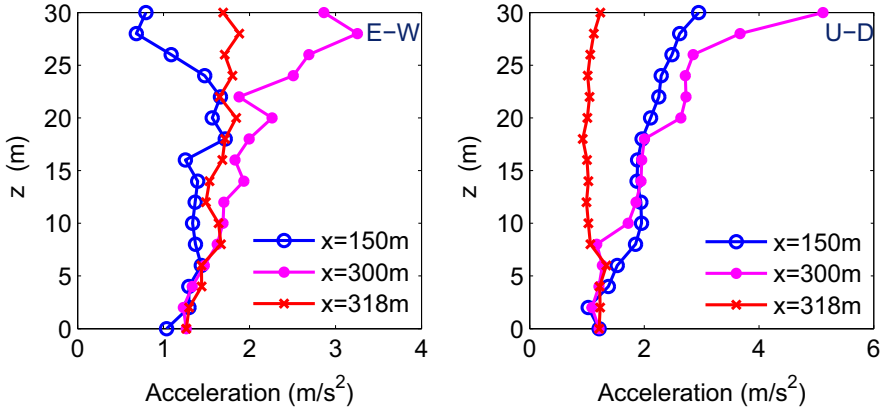

Fig. 12. Acceleration amplification by the seabed foundation to the input seismic wave.

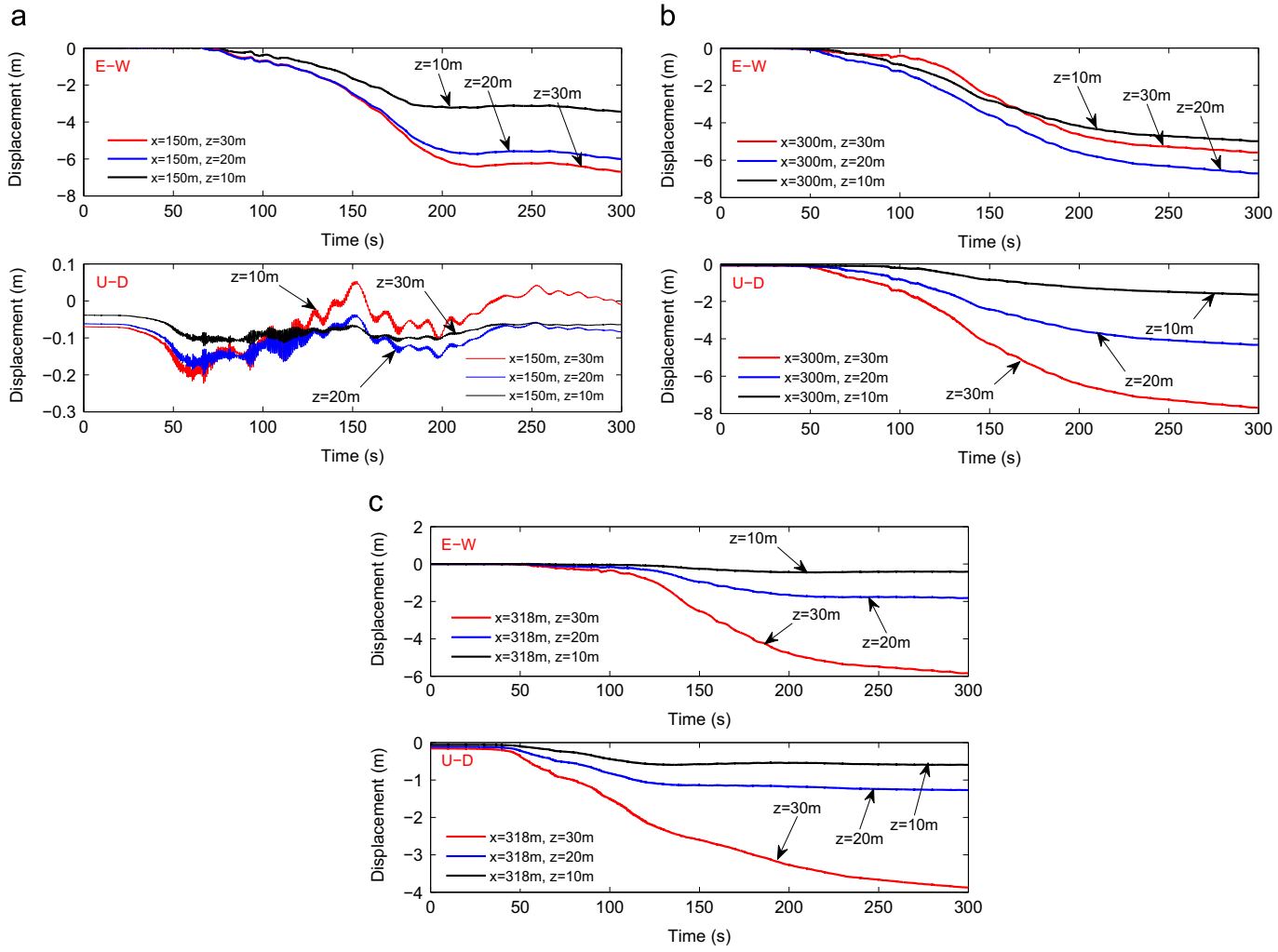

Fig. 13. Time history curve of response displacement in seabed foundation at nine typical positions. (a) $x=150$ m (far field). (b) $x=300$ m (near field). (c) $x=318$ m (symmetric axis).

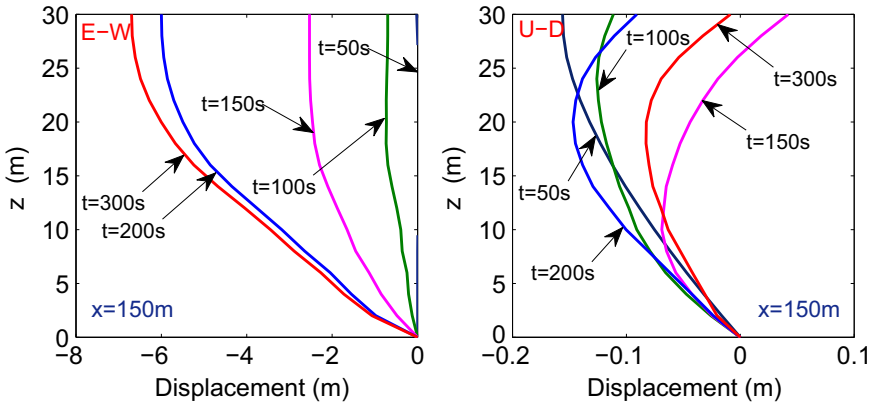

Fig. 14. Displacement distribution along depth in the seabed foundation on line $x=150$ m.

horizontal and vertical accelerations along three typical profiles in the seabed. At the far field ($x=150$ m), the horizontal peak acceleration slightly de-amplifies at the surface, while the vertical amplification linearly increases with soil thickness, reaching up to 3 m/s^2 on the seabed surface. No apparent amplification is observed for vertical peak acceleration at the symmetrical axis $x=318$ m, due to the fact that the weight of composite breakwater could effectively subdue the vertical movement of the seabed soils underneath. It is interesting to observe significant amplification effect along the near-field profile $x=300$ m. The horizontal amplification almost linearly increases with soil thickness from the base, and the peak horizontal acceleration reaches up to about 3 m/s^2 at the seabed surface. The amplification for vertical peak acceleration is nonlinearly developed, with the maximum vertical acceleration reaching up to about 5 m/s^2 at the surface. The amplification of motions along three typical profiles indicates that the presence of the offshore structure can significantly affect the seismic dynamics of seabed foundation. Dynamic interaction between offshore structures and their seabed foundation is intensive and cannot be overlooked.

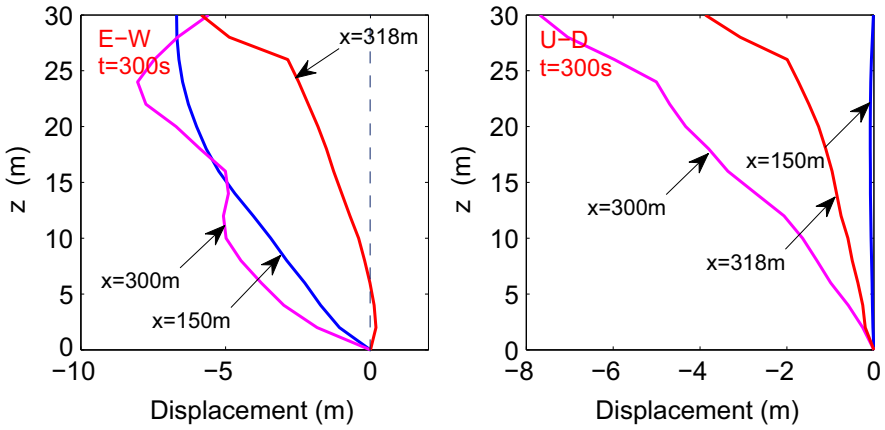

Fig. 15. Displacement distribution along depth in the seabed foundation on line $x=150$ m, 300 m and 318 m.

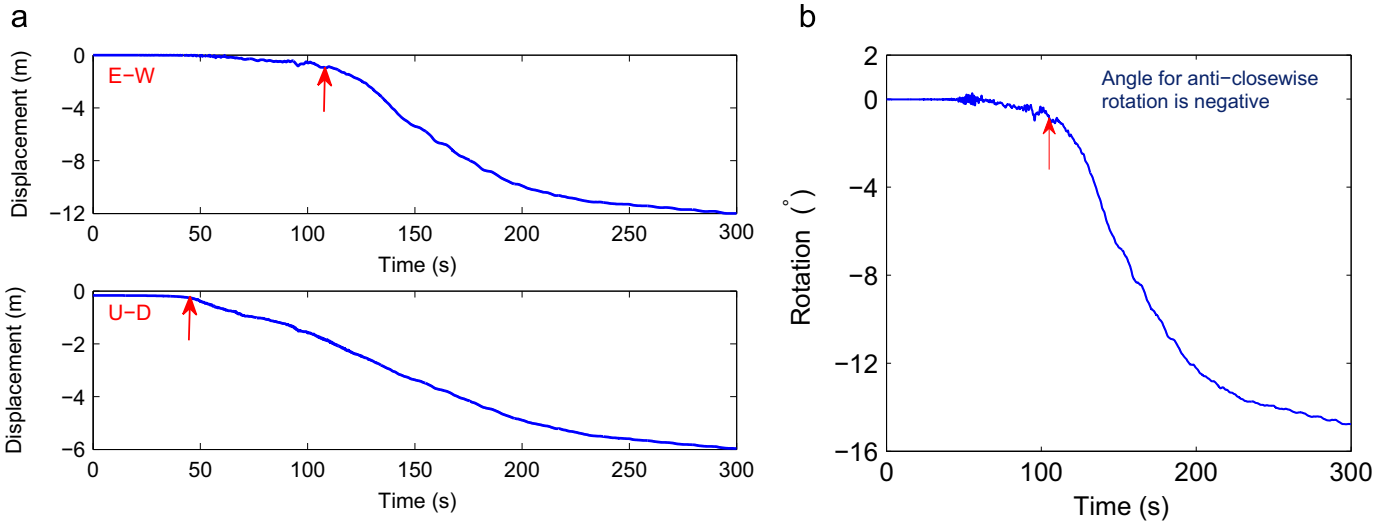

Fig. 16. Response time history of caisson. (a) Displacement. (b) Rotation.

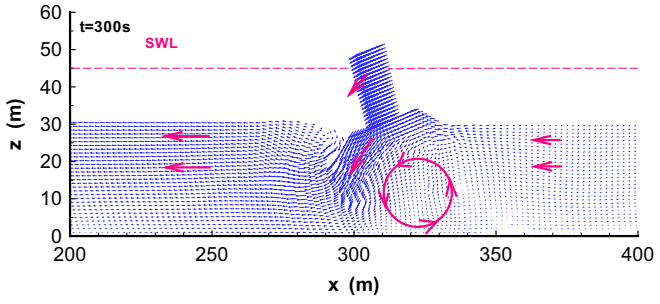

Fig. 17. Displacement vector of breakwater-seabed foundation system at $t=300$ s.

4.2. Displacement profiles

Fig. 13 demonstrates the horizontal and vertical displacement time histories of seabed at nine typical locations at the far field ($x=150$ m), near field ($x=300$ m) and along the line of symmetry ($x=318$ m). Significant lateral displacements in the far field and the near field begin to accumulate at the end of stage 1 ($t=60$ s), when the far-field soil becomes liquefied. The lateral displacement reaches up to 7 m at the end of excitation. However, the vertical displacement at far-field seabed is much less (only in the order of cm). On the other hand, significant vertical movement in the near field and symmetric axis begin to accumulate at the end of stage 1. The lateral displacement at the structural axis only begins to grow substantially at the end of stage 2, when the near-field soil becomes liquefied.

Fig. 14 shows the distribution of horizontal and vertical displacements along the vertical profile in the far field. It is clear that the shape of lateral displacement is nonlinearly developed within the seabed. Peak lateral displacement is attained on the seabed surface, where the gradient of the horizontal displacement is close to zero, indicating there is no shear deformation and shear force acting on the seabed surface. Additionally, fast development of lateral displacement occurs from 100 to 200 s. On the other hand, vertical displacement in the far field is small, and does not follow a clear pattern in distribution.

Fig. 15 further illustrates the displacement field at the end of shaking. In general, the displacements increase with thickness of the soil from the base. The presence of overburden structure apparently reduces the horizontal displacement at the near field. Since the breakwater tilts toward the left when subsiding downward, the vertical displacement on $x=300$ m is much greater than that on $x=318$ m. The vertical displacement at the far field ($x=150$ m) is one order of magnitude smaller than that at the near field.

At the end of the input seismic wave $t=300$ s, the top of the caisson displaces about 12 m to the left and subsides 6 m downward, as shown in Fig. 16. Similar to Fig. 13(c), the caisson begins to settle vertically at the end of stage 1, and starts to displace horizontally at the end of stage 2. At the same time, the caisson gradually tilts anti-closewisely to about 15°. Tilting of the composite breakwater displaces

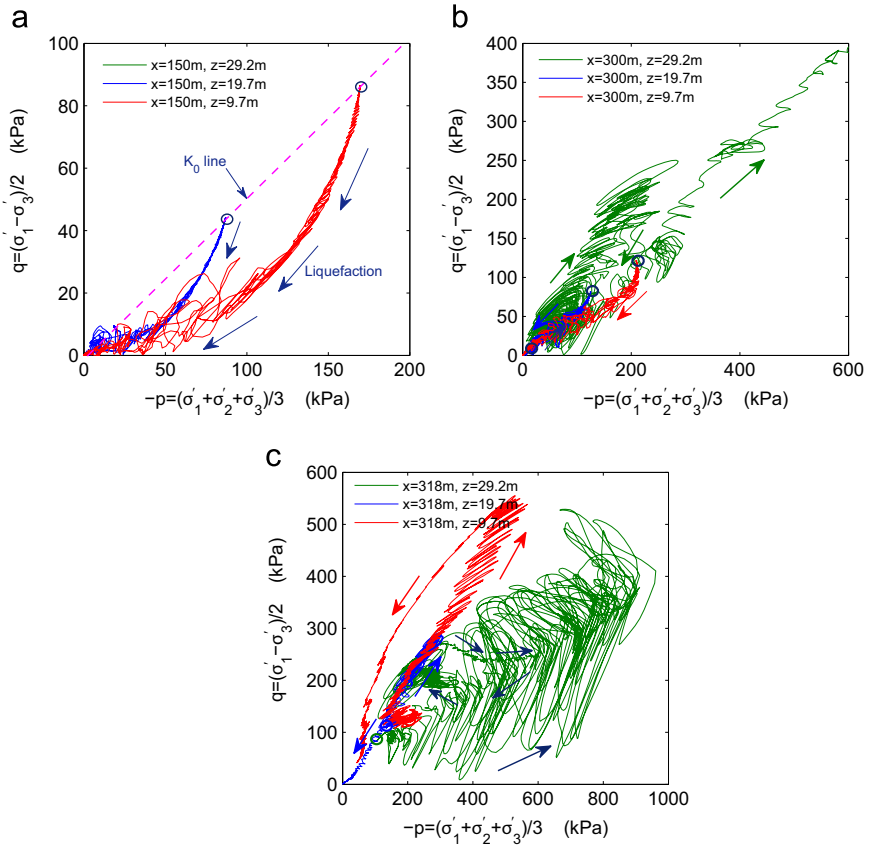

Fig. 18. Effective stress paths on the nine typical positions in seabed foundation. (Note: "○" indicates the initial stress state before shaking). (a) Far-field: $x=150$ m. (b) Near-field: $x=300$ m. (c) Symmetrical axis $x=318$ m.

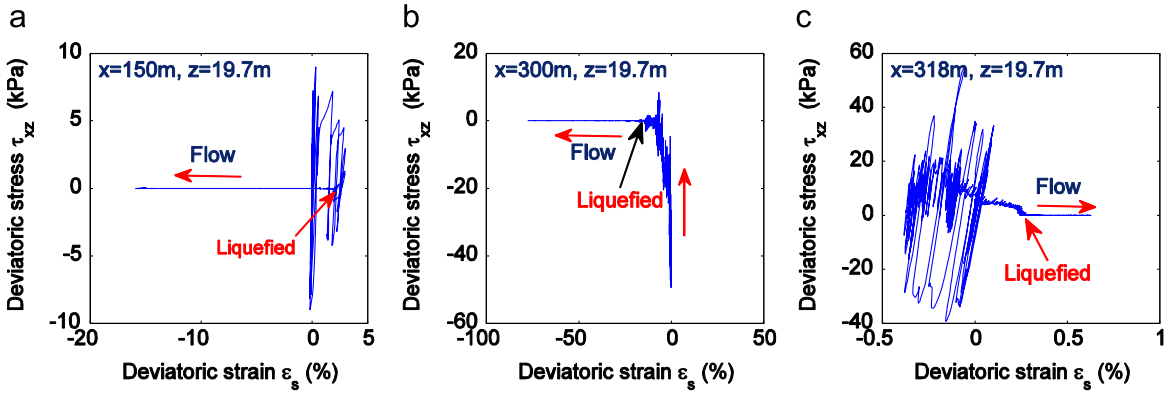

Fig. 19. Stress–strain curves in seabed foundation.

the seabed soil beneath the composite breakwater up to 1 m to right side. As illustrated in Fig. 17, the displacement vector forms an anti-closewise eddy beneath the composite breakwater due to tilting of the breakwater. This displacing mode can effectively block the lateral flow of the liquefied seabed at the right-hand side of the breakwater: the maximum lateral horizontal displacement at the right-hand side of breakwater is only about 3 m, much less than that at the left-hand side of breakwater (about 5–7 m). Accordingly, the soil also heaves upward near the foot of the rubble mound.

4.3. Stress path and nonlinear stress–strain response

In this section, nine positions on three typical profiles are selected as representatives to analyze the effective-stress path and nonlinear stress-strain response of the soils in the liquefaction process at the far field ($x=150$ m), near field ($x=300$ m) and symmetric axis ($x=318$ m). As shown in Fig. 18(a), the initial stress states at the far field are all on the k_0 consolidation line. During the shaking, the effective stress follows a general trend of continuous decrease towards the zero stress state (i.e., liquefaction state). Fig. 18(b)(c) clearly shows that the stress paths of near-field soils are apparently complex due to intensive nonlinear interaction of the soil with the composite breakwater. First, due to the presence of overlying structure, the initial stress states are above the k_0 line at $x=300$ m and $x=318$ m. Additionally, the stress paths in the near fields do not monotonically decrease the same as the far-field condition. In fact, significant increase in the effective mean stress are observed in soils close to the structure ($z=29.2$ m). For near-field soil further away from the composite breakwater($z=19.7$ m), the stress path could approach zero at the later stage of seismic

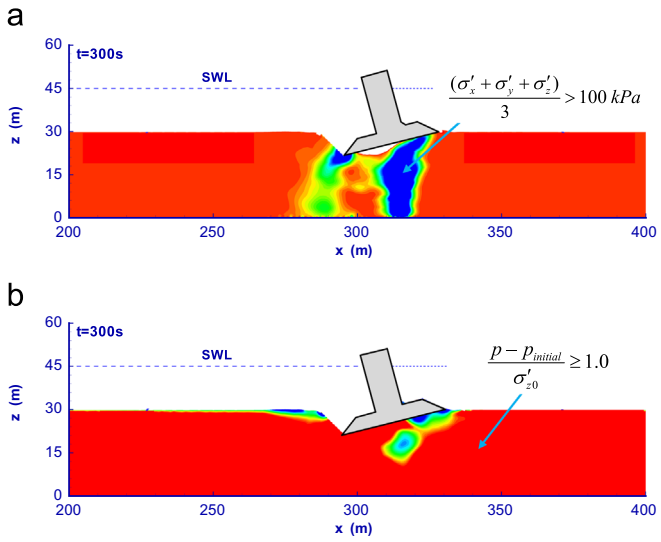

Fig. 20. Comparison of effective stress and residual pore pressure at $t=300$ s in the seabed foundation. (a) Mean effective stresss. (b) Pore pressure ratio.

loading, but not all soils beneath the composite breakwater can be liquefied. The effect of structure can also be clearly observed in the stress-strain curves from Fig. 19. Flow liquefaction results in 15% deviatoric strain in the far-field soil, while only 0.5% deviatoric strain is developed in soils underneath the structure.

5. Conclusions and discussions

In this study, highly nonlinear dynamic interaction of an offshore breakwater and its seabed foundation is investigated using a coupled FEM numerical model. The dynamic behavior of the seabed soil is modeled by using a validated soil constitutive model–Pastor-Zienkiewics Mark III (PZIII) [17,37]. In this investigation, variation of void ratio of the seabed soil and its corresponding permeability, as well as the hydrostatic pressure acting on the surface of seabed and offshore breakwater are updated in each time step in accordance to the seismically induced displacement of offshore breakwater and deformation of the seabed foundation. The practice of numerical implementation indicates that the numerical solution will not converge if these variations are not considered in the numerical modeling, especially in the situation of large-deformation simulation. The computational results show that the developed numerical model FSSI-CAS 2D is capable of capturing the a variety of nonlinear interaction phenomena between the offshore structure and the seabed foundation. It can find important applications in the geotechnical earthquake engineering design of offshore structures.

Comparing with other numerical code, the advantages of numerical code FSSI-CAS 2D used in this study mainly include: (1) the well validated advanced constitutive soil model - PZIII is included, (2) the highly nonlinear interaction between offshore structures and their loose seabed foundation can be simulated effectively using updated Lagrangian approach, (3) the state-dependent variables, such as void ratio e, permeability k, stiffness matrix etc. can be updated in each time step, and (4) the water pressure acting on surface of seabed and offshore breakwater can be automatically updated as the boundary value according to the deformation and displacement of seabed-offshore structures system. The main limitation of the current simulation is that the vibration of breakwater may induce water wave and additional dynamic water pressure, which cannot be simulated at the present stage. Only the hydrostatic water pressure on breakwater and seabed foundation is applied in computation. The effect of this small water wave on the seismic dynamics of offshore structures needs further investigation.

Structures constructed on newly deposited Quaternary sediments could experience excessive subsidence, tilting and rotation under seismic loading due to liquefaction and softening of the seabed soil. The computational results demonstrate intensive, complex nonlinear interaction between offshore structures and their seabed foundation. We observed a three-stage failure mechanism resulted from the seabed and structure interaction. In the first stage, the far-field seabed soil liquefies and reduces confining pressure on the near-field soil. In the second stage, the offshore structure subsides excessively. Presence of the overlying structure postpones liquefaction process of the near-field soil and constrains its dynamic response. Yet, progressive liquefaction of soils close to the structure will eventually cause significant lateral movement and tilting of the structure (the third stage). At the same time, movement of the offshore structures could result in complex variation process of pore pressure, effective stresses, stress path and void ratio in the seabed foundation beneath offshore structures. Through the numerical analysis, significantly different behaviors are observed for the far-field and near-field soils. The difference can only be explained by considering complex interaction between the soil and structure. The analysis also demonstrated that shear wave cannot be transmitted in liquefied soils. This phenomenon proves to some extend that the soil constitutive model PZIII is capable of describing the post-liquefaction behavior of the soil. Once the soil is liquefied, it behaves like heavy fluid.

Analysis in this study shows the composite breakwater translated 12 m horizontally, and subsided 6 m. This composite breakwater could not still serve as the barrier to protect harbor or port. It is suggested construction of offshore structures on loose seabed foundation should be avoided in practice. However, if the situation cannot be avoided, it is highly recommended to evaluate the seismic stability of offshore structures using advanced computational tools, such as the FSSI-CAS 2D program in this study. Ground improvement should be designed to reduce the potential and consequence of seabed liquefaction. Again, advanced numerical tools should be used to evaluate the effectiveness of mitigation measures.

Finally, we remark on two criteria that have been widely used to indicate the degree of liquefaction. Based on physical consideration, the mean effective stress is a direct indicator of liquefaction. In practice, the soil is often regarded as liquefied when the residual pore pressure is equal to or greater than the initial effective pressure. However, the use of pore pressure ratio can be misleading in the cases when intensive soil–structure interaction is involved. Fig. 20(a)(b) compares the distribution of mean effective stress and the pore pressure ratio after the ground shaking. Although the pore pressure ratio for almost all seabed soils are greater than one, the mean effective stresses are still greater than 100 kPa underneath the structure. The discrepancy is due to the fact that the effective pressure is not constant in the near-field area involving complex soil and structure interaction. Accordingly, pore pressure generated within that area can well exceed the initial effective pressure even through the soil is not fully liquefied. Therefore, the pore pressure ratio is not a reliable indicator for liquefaction if the stress state of soils are significantly affected by the structure.

Acknowledgments

The authors thank Professor Andrew Chan in Federation University of Australia for providing computer code of PZIII model. Financial support from Hong Kong Research Grants Council RGC 620311 and HKUST Postdoctoral Matching Fund, and funding from National Natural Science Foundation of China under Project 414 72291 are highly appreciated.

References

[1] Ye JH. Numerical analysis of wave-seabed-breakwater interactions [Ph.D. thesis], University of Dundee, Dundee, UK, May 2012.
[2] Memos C, Protonotarios JN. Patras breakwater failure due to seismic loading. In: Proceedings of the coastal engineering conference, vol. 3; 1993. pp. 3343–56.
[3] Iai S, Kameoka T. Finite element analysis of earthquake induced damage to anchored sheet pile quay walls. Soils Found 1993;33(1):71–91.
[4] Sugano T, Kaneko H, Yamamoto S. The 1999 Ji–Ji earthquake, Taiwan, investigation into the damage to civil engineering structures. In: Damage to port and harbor facilities. Japanese Society of Civil Engineers; 1999 [chapter 5].
[5] Sumer BM, Kaya A, Hansen NEO. Impact of liquefaction on coastal structures in the 1999 Kocaeli, Turkey earthquake. In: Proceedings of the international offshore and polar engineering conference, vol. 12; 2002. p. 504–11.
[6] Yuksel Y, Cetin KO, Ozguven O, Isik NS, Cevik E, Sumer BM. Seismic response of a rubble mound breakwater in Turkey. Proc Inst Civil Eng: Marit Eng 2004; 157(4):151–61.
[7] Katopodi I, Iosifidou K. Impact of the Lefkada earthquake 14-08-2003 on marine works and coastal regions. In: Proceedings of 7th panhellenic geographical conference, Mytilene, Greece; 2004. p. 363–70.
[8] Kiara A, Memos C, Tsiachris A. Some practical aspects on the seismic behavior of rubble-mound breakwaters. In: Ports 2001: America's ports – gateways to the global economy – Proceedings of the ports 2001 conference, vol. 108; 2004. p. 1–10.
[9] Memos C, Bouckovalas G, Tsiachris A. Stability of rubble-mound breakwaters under seismic action. In: Coastal engineering 2000 – Proceedings of the 27th international conference on coastal engineering, ICCE 2000, vol. 276; 2000. p. 1585–98.
[10] Ozaki R, Nagao T. Verification of seismic stability of caisson type breakwater. In: Proceedings of the 13th world conference on earthquake engineering; 2004, Paper no.:0588.
[11] Mohajeri M, Ichii K, Tamura T. Experimental study on sliding block concept for caisson walls. J Waterw Port Coast Ocean Eng 2004;130(3):134–42.
[12] Memos CD, Kiara A, Pavlidis E. Coupled seismic response analysis of rubble-mound breakwaters. Proc Inst Civil Eng: Water Marit Eng 2003;156(1):23–31.
[13] Jafarian Y, Alielahi H, Abdollahi AS, Vakili B. Seismic numerical simulation of breakwater on a liquefiable layer: Iran LNG port. Electron J Geotech Eng 2010;15 D:1–11.
[14] Byrne P. A cyclic shear-volume coupling and pore-pressure model for sand. In: 2nd International conference on recent advances in geotechnical earthquake engineering and soil dynamics, vol. 1.24; 1991. p. 47–55.
[15] Cihan K, Yuksel Y, Berilgen EOCM. Behavior of homogenous rubble mound breakwaters materials under cyclic loads. Soil Dyn Earthq Eng 2012;34 (1):1–10.
[16] Iai S, Ichii K, Liu H-L. Effective stress analysis of port structures. Soils Found (Special Issue of Geotechnical Aspects of the January 17, 1995 Hyogoken-Nambu Earthquake) 1998;(2):97–114.
[17] Pastor M, Zienkiewicz OC, Chan AHC. Generalized plasticity and the modelling of soil behaviour. Int J Numer Anal Methods Geomech 1990;14:151–90.
[18] Elgamal A, Yang Z, Parra E, Ragheb A. Modeling of cyclic mobility in saturated cohesionless soils. Int J Plast 2003;19(6):883–905.
[19] Yang Z, Elgamal A, Parra E. Computational model for cyclic mobility and associated shear deformation. J Geotech Geoenviron Eng 2003; 129(12):1119–27.
[20] Wang ZL, Makdisi FI, Egan J. Practical applications of a nonlinear approach to analysis of earthquake-induced liquefaction and deformation of earth structures. Soil Dyn Earthq Eng 2006;26(2–4):231–52.
[21] Taiebat1 M, Dafalias YF. Sanisand: simple anisotropic sand plasticity model. Int J Numer Anal Methods Geomech 2008;32(8):915–48.
[22] Yin ZY, Chang C. Stress-dilatancy behavior for sand under loading and unloading conditions. Int J Numer Anal Methods Geomech 2008; 32(8):915–48.
[23] Wang G, Xie Y. Modified bounding surface hypoplasticity model for sands under cyclic loading. J Eng Mech 2014;140(1):91–104.
[24] Ye JH. Seismic response of poro-elastic seabed and composite breakwater under strong earthquake loading. Bull Earthq Eng 2012;10(4):1609–33.
[25] Ye JH, Jeng D-S. Earthquake induced dynamic response of 3d poro-elastic unsaturated seabed under a rubble mound breakwater. Soil Dyn Earthq Eng 2013;44(1):14–26.
[26] Zienkiewicz OC, Chang CT, Bettess P. Drained, undrained, consolidating and dynamic behaviour assumptions in soils. Geotechnique 1980;30(4):385–95.
[27] Ye JH, Jeng D-S, Wang R, Zhu C. Validation of a 2-D semi-coupled numerical model for fluidstructure seabed interaction. J Fluids Struct 2013;42:333–57.
[28] Zienkiewicz OC, Chan AHC, Pastor M, Schrefler BA, Shiomi T. Computational geomechanics with special reference to earthquake engineering. England: John Wiley and Sons; 1999.
[29] Xie Y, Wang G. A stabilized iterative scheme for coupled hydro-mechanical systems using reproducing kernel particle method. Int J Numer Methods Eng 2014;99(11):819–43.
[30] Wang G, Sitar N. Static and dynamic axial response of drilled piers. II: numerical simulation. J Geotech Geoenviron Eng 2011;137(12):1143–53.
[31] Taylor DW. Fundamentals of soil mechanics. New York: John Wiley and Sons; 1948.
[32] Casta A. Permeability-porosity relationship: a reexamination of the Kozeny–Carman equation based on a fractal pore-space geometry assumption. Geophys Res Lett 2006;33:2318–22.
[33] Miyamoto J, Sassa S, Sekiguchi H. Progressive solidification of a liquefied sand layer during continued wave loading. Géotechnique 2004;54(10):617–29.
[34] Simo JC, Hughes TJR. Computational inelasticty. New York, Berlin, Heidelberg: Springer-Verlag; 1998.
[35] Ye JH. Numerical modelling of consolidation of 2-D porous unsaturated seabed under a composite breakwater. Mechanika 2012;18(4):373–9.
[36] Ye JH, Jeng D-S, Chan AHC. Consolidation and dynamics of 3D unsaturated porous seabed under rigid caisson breakwater loaded by hydrostatic pressure and wave. Sci China — Technol Sci 2012;55(8):2362–76.
[37] Pastor M, Chan AHC, Mira P, Manzanal D, Fernndez MJA, Blanc T. Computational geomechanics: the heritage of Olek Zienkiewicz. Int J Numer Methods Eng 2011;87(1–5):457–89.